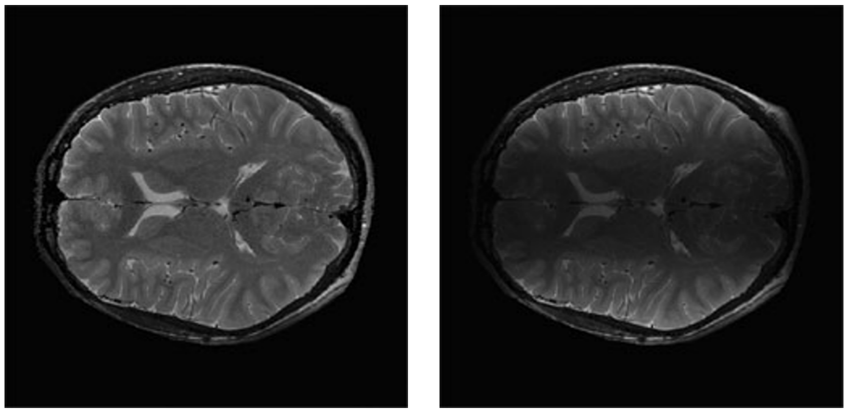

(a) (b)

Figure 1. Effects of inhomogeneity in MRI images of brain: (a) images without inhomogeneity; (b) with inhomogeneity effects.

Figure 2. Illustration of streak artifacts in CT images.

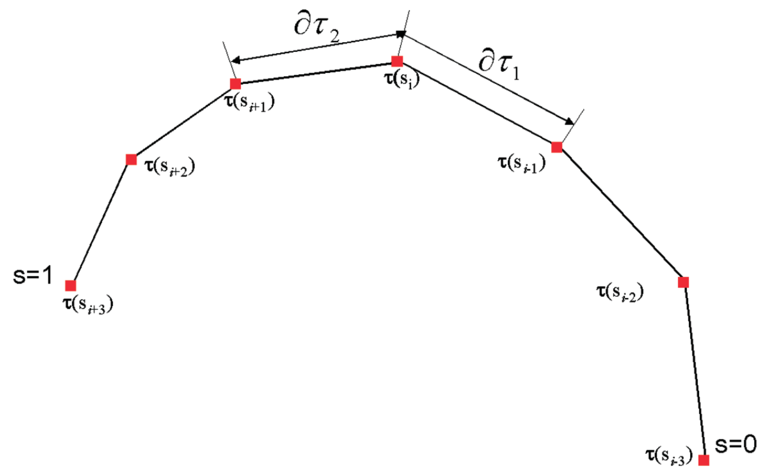

Figure 3. Illustration of computation of the surface tension and rigidity energies in the parametric snake framework.

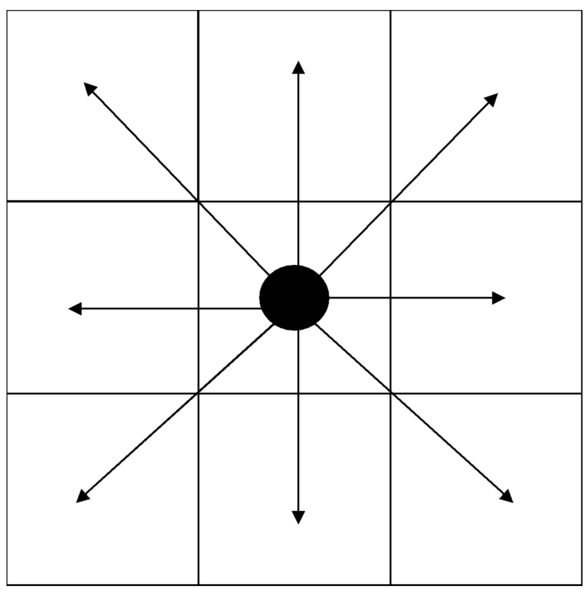

Figure 4. Neighborhood search for the minimum energy configuration.

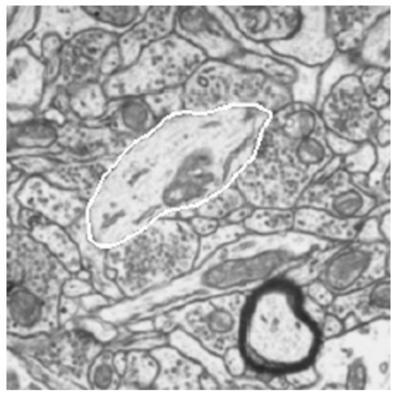

Figure 5. Illustration of segmentation of cellular structure in an EM photomicrograph. Reprinted with permission from [16]. Copyright ©1994, IEEE.

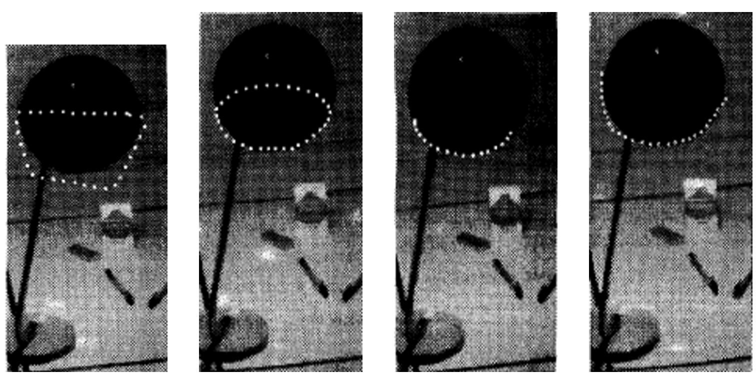

(a) (b) (c) (d)

Figure 6. Illustration of snake-growing algorithm in comparison to conventional snake. (a) Initial contour shown in white dots. (b) Result of conventional snake. (c–e) Performance of snake-growing algorithm. Reprinted with permission from [18]. Copyright ©1990, IEEE.

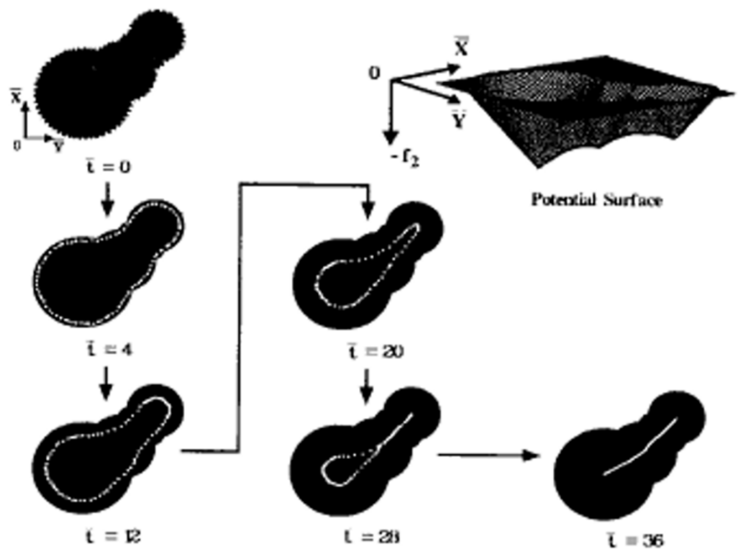

Figure 7. Example of grassfire propagation using an active contour model. The potential surface shows the valley in the distance transform function. Other images show the evolution of the snake toward the skeleton of the object. Reprinted with permission from [19]. Copyright ©1992, IEEE.

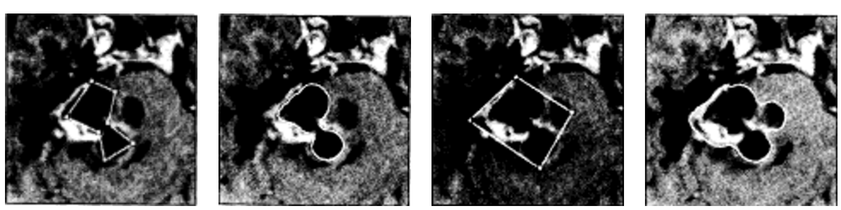

(a) (b) (c) (d)

Figure 8. Illustration of dynamic discrete contour evolution on a cropped region from an MR image of brain. (a,c) Initial contour drawn manually. (b,d) Segmentation result from the contours of (a) and (c), respectively. Reprinted with permission from [20]. Copyright ©1995, IEEE.

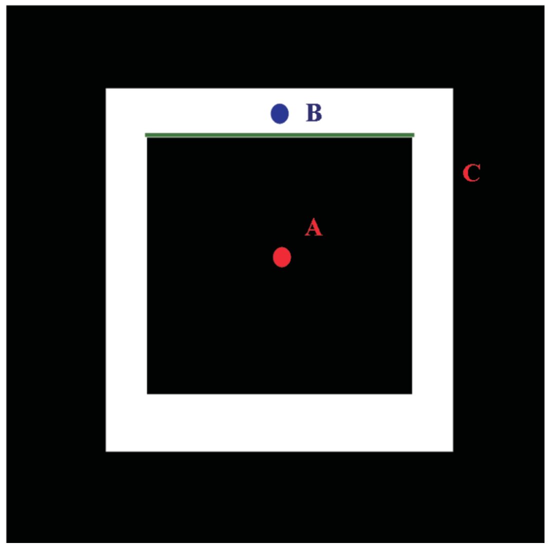

Figure 9. Illustration showing step-up and step-down edges from the observer's point of view.

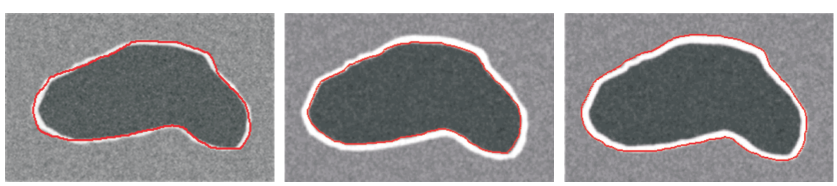

Figure 10. Illustration of gradient orientation on snake deformation: (a) contour deformation without gradient orientation information; (b) segmentation of region when foreground intensity is less than background and (c) when foreground intensity is greater than background intensity. In both (b) and (c) the contour has properly latched onto the desired boundary. Reprinted with permission from [24]. Copyright ©2004, SPIE.

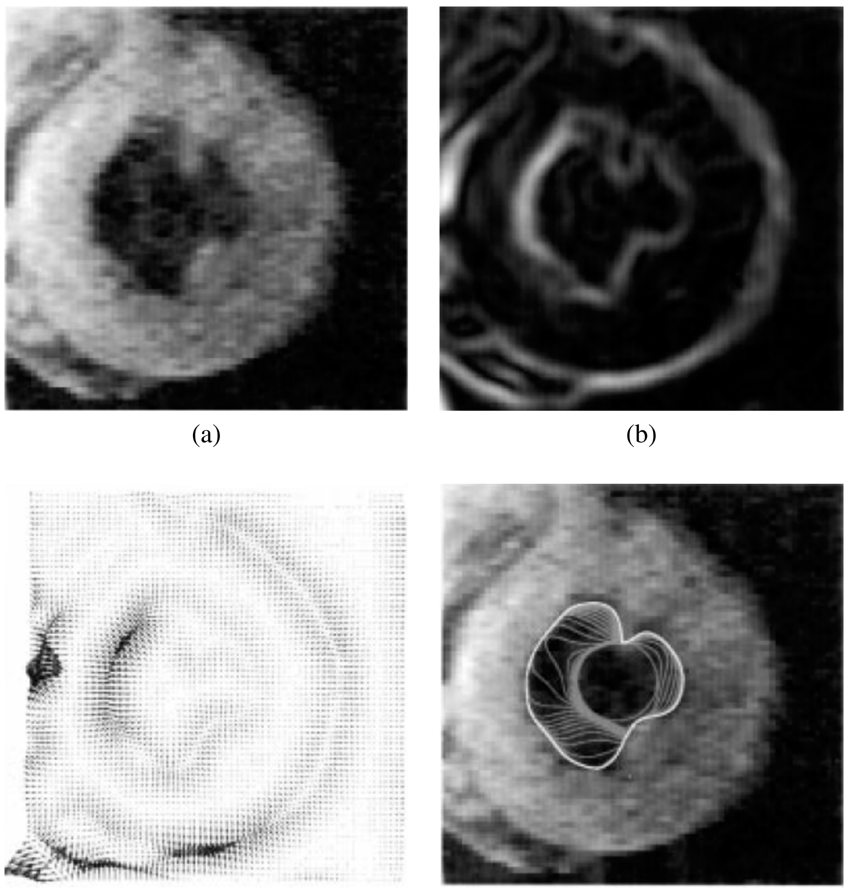

(a) (b) (c) (d)

Figure 11. Illustration for performance of gradient vector flow (GVF) snake in segmentation of left ventricle from an MR image of heart: (a) original MR image showing left ventricle; (b) gradient map derived from (a); (c) vector flow field of the gradient map; (d) segmentation result using GVF snake. Reprinted with permission from [25]. Copyright ©1998, IEEE.

(a) (b)

Figure 12. Images showing the performance of the inertial snake on (a) computer-generated phantom image and (b) ultrasound image of an artery of the lower limb [26].

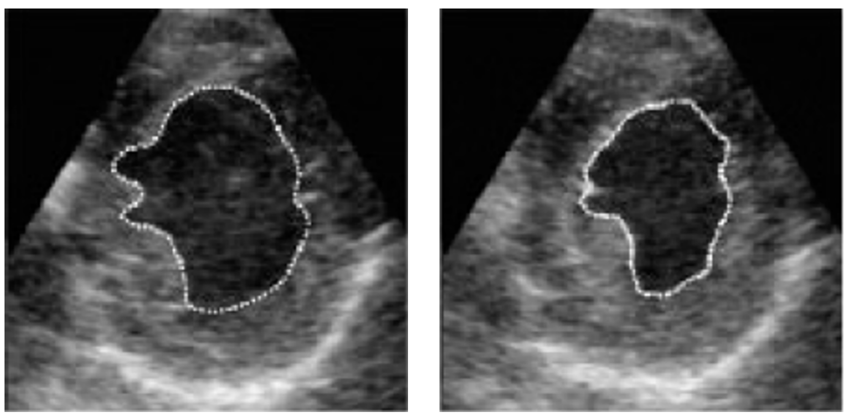

(a) (b)

(c) (d)

Figure 13. Images showing tracking of (a,b) endocardial boundary using the active contour model and (c,d) the mitral valve leaflet boundary. Reprinted with permission from [28]. Copyright ©1998, IEEE.

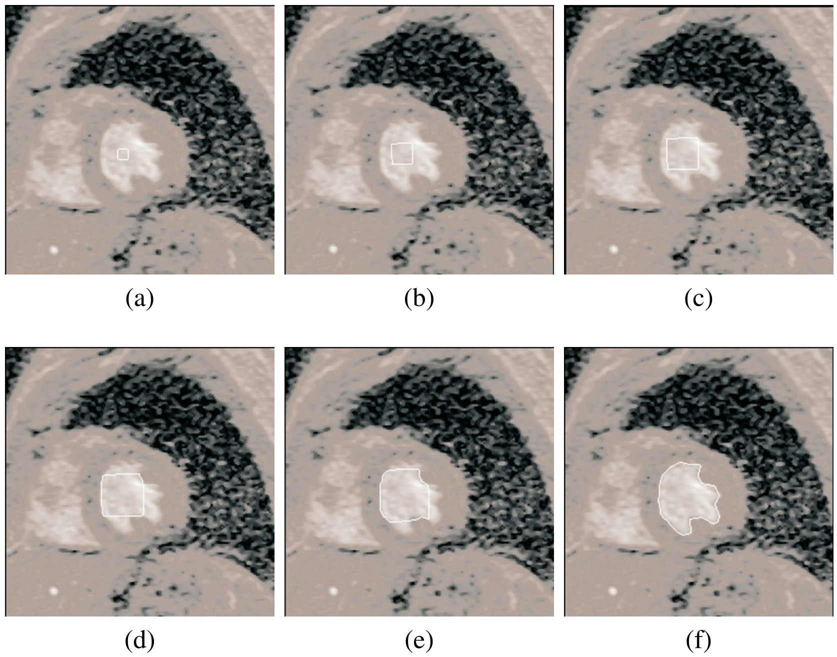

Figure 14. Evolution of region information-based snake for left ventricle segmentation from MR images. The homogeneity parameter is used in conjunction with the other standard energy functions, like geometric and edge functional, to evolve to the final contour, as shown by the white line in (g) from the initial contour in (a). Reprinted with permission from [29]. Copyright ©1997, Institute of Physics.

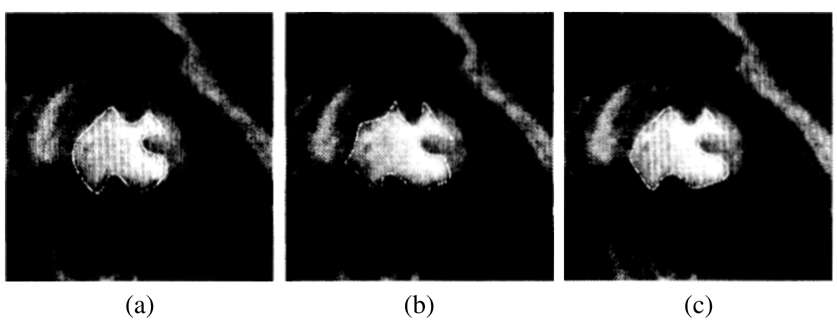

Figure 15. Illustration delineation of endocardium of heart using different methodologies: (a) manual segmentation by an expert; (b) semi-automated segmentation using only the gradient information into the deformable model; (c) same as (b) but with the regional information integrated along with geometric and gradient information. Reprinted with permission from [35]. Copyright ©1994, IEEE.

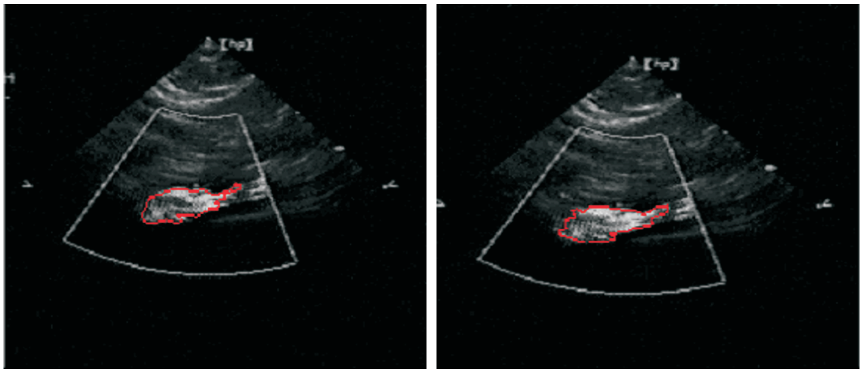

(a) (b)

Figure 16. Illustration of homogeneity-induced inertial snake [32] in segmentation of Doppler ultrasound images.

(a) (b) (c)

Figure 17. Illustration of using shape-based prior in the deformable model framework: (a) shape priors with the mean shape and with a standard deviation around one parameter; (b,c) results of [38] on synthetic images. Reprinted with permission from [38]. Copyright ©1992, IEEE.

(a) (b)

Figure 18. Illustration of the result of dual active contour model (a) initialization of the two contours (shown in white); (b) result after convergence. Reprinted with permission from [47]. Copyright ©1997, IEEE.

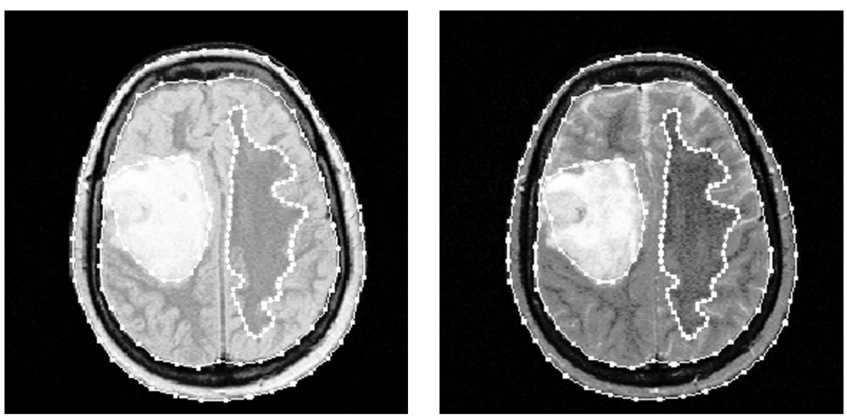

(a) (b)

Figure 19. Segmentation results in sections of NMR images of brain using statistical snake. Reprinted with permission from [31]. Copyright ©1994, British Machine Vision Association Press.

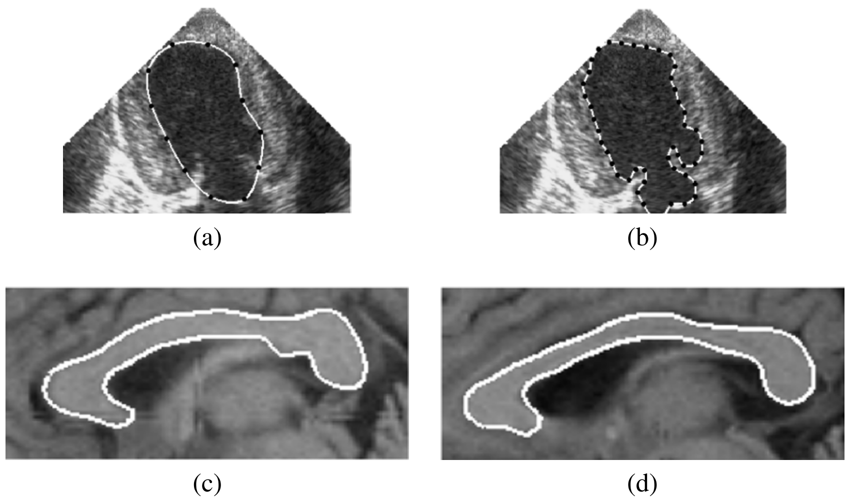

Figure 20. Segmentation results using the probabilistic model proposed in [48]: (a) initial contour drawn on an ultrasound image of dog heart; (b) final segmentation result; (c,d) segmentation of corpus callosum from MR images. Reprinted with permission from [48]. Copyright ©2004, IEEE.

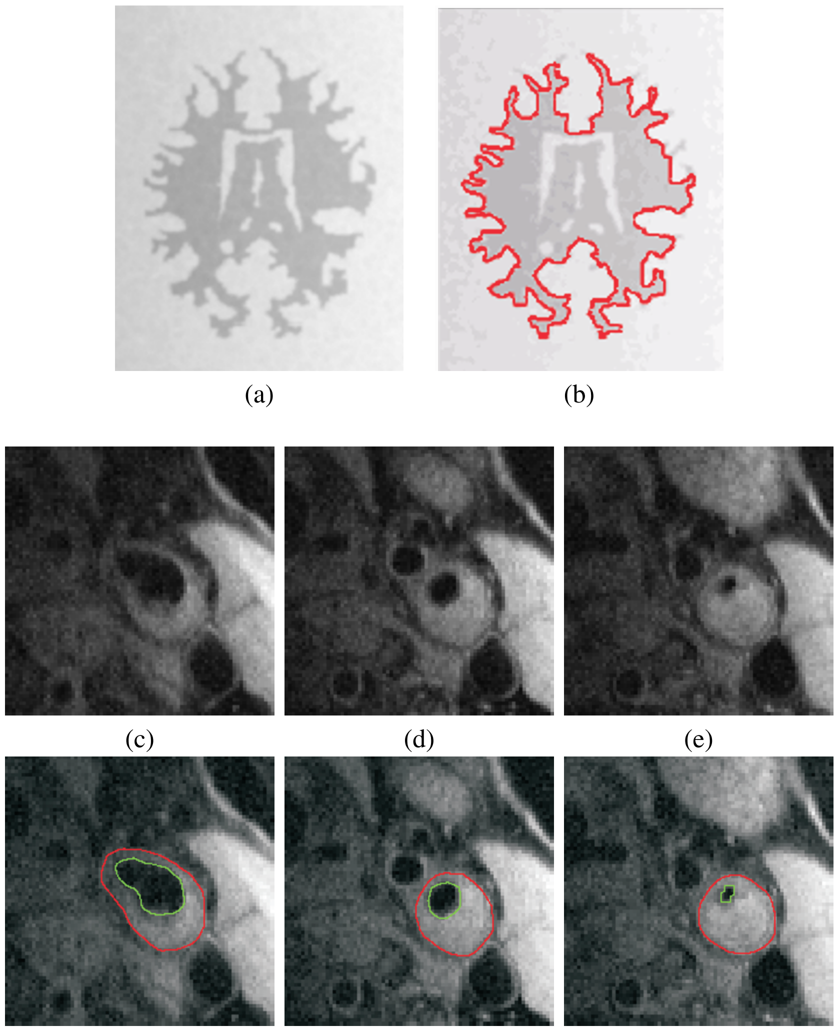

(a) (b) (c) (d) (e) (f) (g) (h)

Figure 21. Illustration of class uncertainty-induced snake: (a) phantom image generated from segmented mask of brain with noise and inhomogeneity added; (b) segmentation using class uncertainty-induced active contour [49]; (c–e) cropped region showing carotid artery in MR images (courtesy Hospital of the University of Pennsylvania); (f–h) segmentation of lumen (green) and outer vessel wall (red) using the class uncertainty based snake.

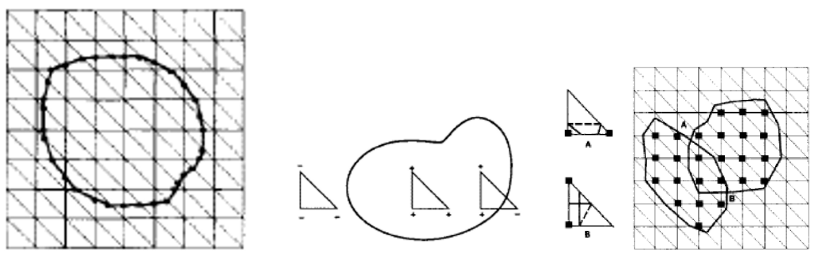

(a) (b) (c)

Figure 22. (a) Simplicial approximation of contour model using a Freudenthal triangulation [59]. (b) Cell classification. (c) Intersection of two snakes with "inside" grid cell vertices marked. Snake nodes in triangles A and B are reconnected. Reprinted with permission from [59]. Copyright ©1995, IEEE.

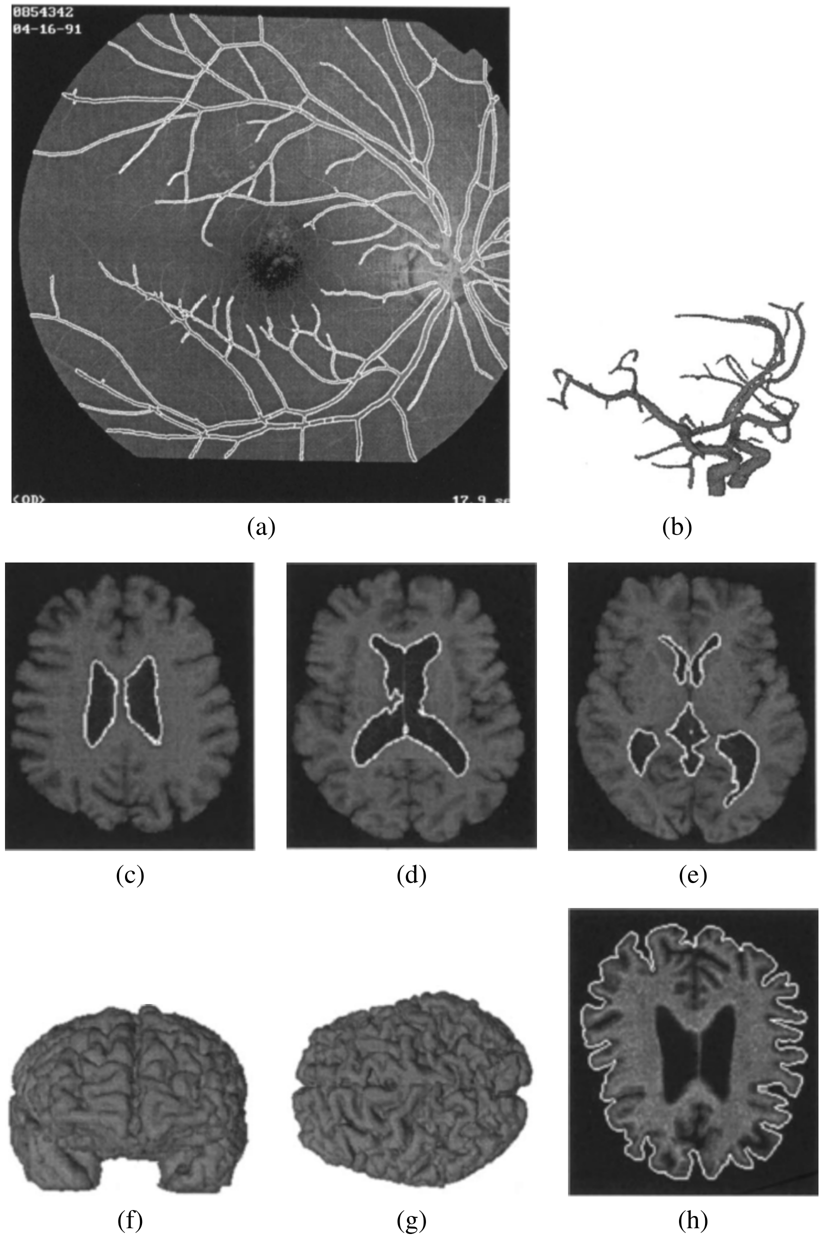

Figure 23. Illustration of results of segmentation using topology-adaptive active contour model on 2D images and 3D volumes [60]. (a) Segmentation of blood vessels in retinal angiography. T-surface segmentation of (b) cerebral vasculature from MR image volume; (c–e) ventricles from MR image volume of the brain; (f–h) different view of cerebral cortex segmentation using T-surface. Reprinted with permission from [60]. Copyright ©1999, IEEE.